

Lab on a Chip

Accepted Manuscript



This is an *Accepted Manuscript*, which has been through the Royal Society of Chemistry peer review process and has been accepted for publication.

Accepted Manuscripts are published online shortly after acceptance, before technical editing, formatting and proof reading. Using this free service, authors can make their results available to the community, in citable form, before we publish the edited article. We will replace this *Accepted Manuscript* with the edited and formatted *Advance Article* as soon as it is available.

You can find more information about *Accepted Manuscripts* in the [Information for Authors](#).

Please note that technical editing may introduce minor changes to the text and/or graphics, which may alter content. The journal's standard [Terms & Conditions](#) and the [Ethical guidelines](#) still apply. In no event shall the Royal Society of Chemistry be held responsible for any errors or omissions in this *Accepted Manuscript* or any consequences arising from the use of any information it contains.

Artery-on-a-chip platform for automated, multimodal assessment of cerebral blood vessel structure and function

Sanjesh Yasotharan,^{1,2} Sascha Pinto,² John G. Sled,^{3,4} Steffen-Sebastian Bolz^{5,6,7}
and Axel Günther^{1,2}

¹Department of Mechanical and Industrial Engineering, University of Toronto,
5 King's College Road, Toronto, Ontario, M5S3G8, Canada

²Institute of Biomaterials and Biomedical Engineering University of Toronto,
164 College Street, Toronto, Ontario, M5S 3G9, Canada

³Department of Medical Biophysics, University of Toronto, Toronto Medical Discovery
Tower, MaRS Centre, 101 College Street, Toronto, Ontario M5G 1L7, Canada

⁴Hospital of Sick Children, Mouse Imaging Centre, 25 Orde Street, Toronto,
Ontario M5T 3H7, Canada

⁵Department of Physiology, University of Toronto, 1 King's College Circle, Toronto,
Ontario, M5S 1A8, Canada

⁶Toronto Centre for Microvascular Medicine, University of Toronto,
and Li Ka Shing Knowledge Institute, St. Michael's Hospital, 209 Victoria Street, Toronto,
Ontario, M5B 1T8, Canada

⁷Heart and Stroke/Richard Lewar Centre of Excellence in Cardiovascular Research,
101 College Street, Toronto, Ontario, M5G 1L7, Canada

Abstract

We present a compact microfluidic platform for the automated, multimodal assessment of intact small blood vessels *in vitro*. Mouse olfactory artery segments were reversibly loaded onto a microfluidic device and kept under physiological (i.e., close to *in vivo*) environmental conditions. For immunohistochemical endpoint protein analysis, automated *on chip* fixation and staining of the artery eliminated the need for any subsequent tissue sectioning or processing outside the chip. In a first case study, we demonstrate the blood vessel abluminal structure based on the positions of

smooth muscle cell nuclei, actin filaments and voltage gated calcium channels. In a second case study we incubated smooth muscle cells (SMCs) with a calcium-sensitive dye allowed to simultaneously assess time-dependent, agonist-induced calcium and diameter changes of pressurized resistance arteries. We expect the presented microfluidic platform to promote routine on-chip staining and quantitative fluorescence imaging of intact blood vessels from different vascular beds, tissue engineered vascular constructs and vascularized microtissues. The at least tenfold reduction in required aliquot volumes for functional assessment and staining was achieved by on-board fluid manipulation of the syringe-pump free platform and may promote its applications for screening of newly synthesized compounds.

Keywords: organs-on-a-chip, artery-on-a-chip, olfactory blood vessel, immunohistochemistry, tissue processing

1. Introduction

In a wide range of biological applications, microfluidic devices have demonstrated their ability for exquisite spatiotemporal manipulation of physicochemical microenvironments in manners that closely resemble *in vivo* conditions, reduce reagent consumption and are automatable.^{1, 2} Such microphysiological or “organ-on-a-chip” platforms³⁻⁵ are based on animal or human cells and provide *in vitro* models that recapitulate aspects of the structure and function associated with intact tissues and organs. Microphysiological systems have been demonstrated for the liver,^{6,7-9} the lung,¹⁰⁻¹² the kidney,¹³⁻¹⁵ the gut,¹⁶ the intestine,¹⁷ the heart^{18, 19} and the pancreas.^{20, 21} Several of these bottom-up approaches relate to blood vessels, particularly to the formation of perfused capillary networks²²⁻²⁷ and the effect of

fluid shear stress exerted on endothelial cells (ECs).²⁸ Microphysiological systems allowing vascular cell contractility and calcium dynamics start becoming available.²⁹ Conventional approaches for characterizing the structure and function of intact blood vessels relied on imaging their diameter either *ex vivo*,³⁰ as in the case of pressure myography, or *in vivo*.³¹ Our group has previously developed the first approach that allows intact small blood vessels to be reversibly hosted on a microfluidic device while being subjected to physiological levels of transmural pressure and temperature.³² The intactness of the smooth muscle cell (SMC) and EC layers of a chip-hosted mouse mesenteric artery segment was assessed during the acquisition of the diameter change, D , in response to abluminal stimulation with phenylephrine (PE) and acetylcholine (Ach), respectively.

Here, we report an extended artery-on-a-chip platform that allows a blood vessel segmented to be reversibly hosted and calcium dynamics to be simultaneously assessed with vascular tone. The vessel segment can be fixated and staining protocols applied *on chip*. Figure 1A illustrates our experimental approach. Chip hosted blood vessel segments are manually isolated and subjected to constant levels of physiological temperature and transmural pressure. On the abluminal side, the vessels are exposed to a chemical milieu that may either be constant or vary with time. Blood vessel diameter and calcium signals are dynamically recorded from bright field and ratiometric fluorescence images, respectively. End-point analyses performed on the chip-hosted blood vessels after fixation, staining and fluorescence imaging reveal nucleic acid and protein level information. Automated microfluidic approaches have been introduced for perfusion culture,³³ and immunohistochemistry of cells^{2,}³⁴ and tissue constructs.³⁵

Here, we utilize mouse olfactory arteries with a resting outer diameter, D_{max} , of approximately 120 μ m. The cerebral resistance arteries originate from the anterior parts of the brain and regulate blood flow into the olfactory bulb region. Figure 1B shows micro computed tomography and magnetic resonance images of the brain vasculature where the location of the olfactory artery is indicated. Figure 1C shows the cross-section of an olfactory artery that consists of one layer of ECs on the luminal side and several layers of circumferentially orientated SMCs, on the abluminal side. Vascular tone is defined as the ratio $(D - D_{max}) / D_{max}$. Our work provides time-resolved measurement of arterial tone concurrently with calcium dynamics,^{22, 36} as well as structural end-point analyses of chip-hosted, pressurized blood vessels. The manual steps for chip-external tissue processing, sectioning, and image reconstruction associated with conventional protocols (Fig. 1D) were eliminated by the presented automated approach (Fig. 1E). On-chip fixation and staining of pressurized blood vessel segments allowed the structure of the blood vessel to be assessed along the circumferential and axial directions, at a well-defined transmural pressure and tone. In contrast, cross-sectional slices of an entire blood vessel segment reveal structural features only in the circumferential direction of the arterial wall. Assessing blood vessel structure in the axial direction based on tissue slices is cumbersome, as it requires merging and processing image data from separate scans of individual tissue slices.

In section 2 we discuss details of the experimental artery-on-a-chip platform along with the employed staining protocols. In section 3 we present measurements of vasomotor and intracellular calcium responses performed on olfactory artery segments that were incubated with a ratiometric calcium indicator dye. We also report automated fixation and staining of smooth muscle for f-actin, nuclei and voltage gated calcium channels. In section 4 we

summarize the presented results.

2. Experimental

2.1 Microfluidic Device and Manifold

Figure 2A shows the experimental setup that consists of an artery-on-a-chip microfluidic device, a manifold with solenoid valves, a common gas inlet from a pressure regulator, liquid-filled inlet (perfusion) and outlet (superfusion, fixation) lines, a computer equipped with a data acquisition card, an external power supply and a temperature controller. Six different solutions shown in red, orange, green, blue and yellow colour (see “1” in Fig. 2A, and Fig. 2F) were pre-filled into the wells of the manifold in preparation of automated functional assessment and abluminal staining. Opening the respective on-chip valve initiated outflow from the respective pressurized manifold well into the superfusion channel that was in fluidic contact with the abluminal side of the artery. The schematic shows a rendered image of the artery-on-a-chip device that was fabricated using two-layer soft lithography. The design and fabrication of artery-on-a-chip devices are described in detail in ESI Section S.1 (particularly Figs. S1A-S1C). After isolation, an approximately 1mm long olfactory vessel segment was manually inserted into the loading well. By controllably withdrawing fluid at the perfusion inlet the vessel segment flowed through the loading channel until it reached the desired position in the inspection area. Figure 2B shows the inspection section of the artery-on-a-chip device. The microchannel network shown in blue color served to reversibly connect the two ends of the artery segment to the inspection section of the microfluidic device. After a sub-atmospheric pressure, P_{fix} , was applied, the arterial wall at the fixation locations complied with the rectangular cross section of the microchannel. The artery segment was therefore immobilized and unwanted cross talk was prevented

between the solutions in contact with the luminal side (i.e., the perfusion stream, labelled in green color) and the abluminal side (i.e., the superfusion stream, labelled in red color) in the presence of an applied transmural pressure, P_{perf} . The loading well was then sealed by a lid. Physiological levels of transmural pressure (45mmHg) were established by closing the perfusion outlet connected to the lid and by the elevating the perfusion inlet reservoir. The top and the bottom sections of the arterial wall of a pressurized olfactory artery segment resided between two horizontal walls that were decorated with arrays of equidistantly spaced pillars. The perfusate passed through the manifold and further through the perfusion channel (shown in green color in Fig. 2A) where it contacted the luminal side of the artery. In difference to the inspection section of our earlier artery-on-a-chip device for functional assessment of mesenteric arteries,³² the present design allows the abluminal side of the arterial wall to be superfused in cross-flow while the pillar-supported regions of the arterial wall remained within the same focal plane. Figure 2C shows a bright-field photograph of a fixated and pressurized mouse olfactory artery segment with an outer diameter of $\sim 120\mu\text{m}$, approximately half the size of previously studied mesenteric arteries. Olfactory arteries are surrounded by less connective tissue as compared to mesenteric arteries, allowing the extracellular matrix to be nearly completely removed during the manual dissection and vessel isolation steps, and therefore provide undistorted access to stained SMCs. The microfluidic devices contain $70\mu\text{m}$ deep microchannels with the narrowest features being the $60\mu\text{m}$ wide artery immobilization channels in the inspection area (Fig. 2B).

Figure 2D shows a cross sectional view of the inspection area with the array of $20\mu\text{m}$ diameter and $30\mu\text{m}$ tall pillars (center-to-center spacing of $40\mu\text{m}$) covering the top and the bottom walls. While flowing across the abluminal side of the artery, the superfusion stream

passes through the void regions in between pillars. The reduction in cross sectional area exposes the SMCs to increased shear levels in the pillar-supported regions of the arterial wall. Superfusion flow rates were up to 0.5 μ l/min, corresponding to a maximum centerline velocity of 3.1 mm/s within the superfusion channel, a pressure drop across the vessel of approximately 8 Pa (0.06 mmHg, or 0.1% of the transmural pressure), and a numerically estimated peak shear stress at the top/bottom sections of the arterial wall of 5.6 dyne/cm² (Fig. 2E, for detail see section ESI S5). The associated wall shear stress fell within the range experienced by SMCs *in vivo*, due to interstitial fluid flow, and did not exceed levels known to induce vasoconstriction,^{37, 38} or nitric oxide or heme oxygenase³⁹ production in ECs.

Figure 2F shows one of six on-chip valves that allow for the outflow from an individual well on the manifold body into the superfusion channel to be controlled. The characterization of the on-chip valves is discussed in ESI section S3. Figure 2G shows the thin film temperature sensors that measure the temperature in proximity of the artery. The calibration and measurement of the artery temperature is discussed in ESI section S4.

Figure 3A shows photographs of the manifold consisting of a base plate, the manifold body, a lid sealing the artery loading well and a lid sealing the fluid wells. For a detailed description of the manifold design and machining we refer to ESI section S2. Briefly, the manifold body was milled in aluminum and accommodated external connections for the perfusion inlet line, as well as the superfusion outlet and the outlet used for blood vessel fixation. The manifold also accommodated nine 350 μ l liquid fillable wells. A constant head pressure, P_I , was common to all wells and accurately adjusted with a digital pressure regulator. Outflow from six of the nine wells was initiated by electronically addressing individual solenoid valves that were side-mounted to the manifold and selected between the two common pressures levels,

P_{open} and P_{vac} . The six outlets actuated six individual on-chip membrane valves (see “7” in Fig. 2A, and Fig. 2G) and initiated the outflow from one particular well into the superfusion channel.

We employed a reversible interconnect to establish robust fluidic seals between the manifold body and the artery-on-a-chip microfluidic device, as well as between the lid and the artery loading well. Figure 3B shows a cross-section of the configuration where a cylindrical rim with the contact area A_{rim} is positioned coaxially with respect to an inlet or outlet hole of a PDMS based microfluidic device. A force F_A locally applied in the proximity of the fluidic connection. Localizing F_A to a small fraction of the total device surface causes a well-defined deformation of the elastomeric material and therefore establishes a seal. Figure 3C shows the corresponding stress distributions that were numerically predicted from a finite element analysis (Comsol 4.2, Burlington, MA, USA). The edges of the cylindrical rims pressed against the elastomeric device surface and caused stress concentrations in the elastomeric device with peak normal stresses exceeding the average stress applied to the rim surface, $\sigma_{seal}=F_A/A_{rim}$, by approximately 2.5 times (Fig. 3D). As a result, the rim locally deformed the elastomeric device and a consistent seal was obtained.

The seal fails if the internal fluid pressure, P_i , increases to a level where it deforms the PDMS surface in contact with the cylindrical rim to an extent that the normal stress at the interface between the device and the rim vanishes. Increasing F_A will therefore be required to consistently seal at increased pressures. Note that for $P_i > 200\text{kPa}$ (gauge pressure), plasma bonded PDMS devices (using plasma generated under high vacuum) show a decreased yield and may delaminate.^{40, 41} Unnecessarily high values of F_A might compress the device to an extent that internal channel networks (partially) collapse, especially for devices containing

layer thicknesses < 2 mm. The operating envelope for obtaining a consistent seal in terms of F_A , A_{rim} and P_i , is therefore an important requirement for the design and consistent application of the proposed fluidic interconnect.

The sealing mechanism was quantitatively evaluated by applying a constant force F_A up to 30 N, corresponding to σ_{seal} of 1.5MPa using the experimental setup shown in Fig. 3E. The force was established using a pneumatic cylinder (McMaster-Carr, Aurora, OH, USA) that was co-axially attached above the fluidic interconnect (manifold) containing the rim, via a thread. The pressure applied to the pneumatic cylinder was measured with a (100PSI full scale, McMaster-Carr). The working fluids of either compressed air or de-ionized water passed through the interconnect to a PDMS device that was prepared using standard soft lithography and contained a single microchannel with only one inlet and one outlet. To measure P_i , a pressure transducer (30PSI full scale, Honeywell, NJ, USA) was connected to the outlet of the microfluidic device as indicated in Fig. S2.3A. The sealing force F_A was subsequently decreased until a leak was detected by monitoring P_i .

Figure 3F shows the operating envelope obtained for the successful operation of the seal. In line with our expectations, we found comparable seal operating conditions for the two considered fluids of compressed air and distilled water. A linear regression yielded $P_{i,max} = a \cdot \sigma_{seal} + b$ with $a = (176 \pm 13) \times 10^{-3}$ and $b = -(24 \pm 10) \times 10^3$ Pa. Consistent seals were obtained even for applied stresses greater than 1.3 MPa and pressures beyond 200 kPa. However beyond 200kPa devices started to fail due to inconsistencies associated with the PDMS-glass bond.

2.2 Artery Isolation and Functional Assessment

The microfluidic device was placed into the base plate and the main manifold body containing the liquid via screw connections that established the reversible seal. The wells were initially primed with filtered 1% BSA that flowed into all liquid-carrying microchannels, and subsequently with 3-(N-morpholino)propanesulfonic acid (MOPS) buffer. On-chip bubble traps⁴² were operated at 20 in Hg vacuum for the duration of the experiment to eliminate any bubbles. Cerebral olfactory arteries were manually isolated from C57BL/6 mice (Charles River, Wilmington, MA, USA) and loaded onto the chip as previously described for mouse mesentery arteries.³² Upon reaching the inspection area of the device, the loading well was closed with a lid, and the perfusion inlet (“3” in Fig. 2A) was subjected to a hydrostatic head of 45 mmHg while the superfusion outlet well remained at the chip level and was therefore at atmospheric pressure. Superfusion flow of MOPS buffer across the artery segment was supplied at a constant rate of approximately 0.5 $\mu\text{l}/\text{min}$ by controllably pressurizing the head spaces of the liquid wells using digital pressure regulators (model T3410se0g005p000, pressure range 0-5psi, MarshBellofram, Newell, WV, USA). The pressure of the fixation reservoir was kept at a hydrostatic head of 45 mmHg below atmospheric pressure. Vessel segments were heated to a temperature of $37.0 \pm 0.5^\circ\text{C}$ using the temperature control strategy described above and shown in Fig. 2H. Bright field and fluorescent images were obtained on an inverted fluorescence microscope (model Ti Eclipse, Nikon, Japan) with a 20 \times objective (Nikon model CFI S Plan Fluor ELWD 20 \times).

Phenylephrine (PE, Sigma Aldrich, St. Louis, MO, USA) was used to evaluate smooth muscle function, prepared in premixed solutions (0.1 μM , 1 μM , 5 μM , and 10 μM PE in MOPS) and loaded into separate wells (for detailed experimental sequences see ESI S7). To

demonstrate the changes in functional response due to the presence of a drug, the calcium blocker Nifedipine (Sigma Aldrich) was incubated for 30 min at a concentration of $1\mu\text{M}$ in MOPS at 37°C . The artery outer diameter was dynamically recorded using a custom software program (Matlab R2010b, Mathworks, Natick, MA, USA), as previously described.³²

2.3 Small Artery Staining

Nuclei and F-Actin. Artery segments were fixed with 4% methanol-free paraformaldehyde (PFA) at 4°C for 30 min (either by automated TE cooling, or by submerging the entire manifold and device in ice), permeabilized with 0.5% TritonX (Sigma Aldrich) for 30 min, blocked with 1% BSA for 15min and co-incubated with Alexafluor 594 Phalloidin (Invitrogen, Grand Island, NY, USA) for F-actin staining and 4',6-diamidino-2-phenylindole (DAPI) (F. Hoffmann-La Roche, Basel, Switzerland) for nuclear staining for 2 hours at room temperature. An inverted fluorescence microscope (model Nikon Ti Eclipse) with a $40\times$ objective (Nikon CFI S Plan Fluor EWLD $40\times$) and a CCD camera (1392×1040 pixel resolution, model EXi Blue, QImaging, Surrey, BC, Canada) were used for imaging (see ESI Table S7.1 for programmed experimental sequence).

Immunohistochemistry. Immunofluorescence for L-type calcium channels was carried out by incubating a fixed, permeabilized and blocked artery segment in 1:50 diluted Anti $\text{Ca}_v1.2$ (Alomone Labs, Jerusalem, Israel) for 10 hours, followed by 1:1000 diluted Alexafluor568 Anti-rabbit IgG (Invitrogen) for 2hours (see ESI Table S7.2 for programmed experimental sequence).

Intracellular Calcium. Smooth muscle cells of arterial segments were superfused with a $2\mu\text{M}$ FURA2-AM solution (Sigma Aldrich, St. Louis, MO, USA) for 90min at 37.0°C to

load Fura2-AM and to allow for sufficient hydrolyzation of the acetoxymethylester. Excess FURA2-AM was subsequently removed by superfusing MOPS buffer for two minutes prior to imaging and exposure to PE. Fura 2 fluorescence was recorded at excitation wavelengths of 340nm and 380nm, respectively (Lamda LS 175W Xeon light source, Sutter Instruments, CA, USA). Using an electron multiplying charge coupled device (EMCCD) camera (resolution 512×512 pixels, model Evolve512, Photometrics, Tucson, AZ, USA), images were periodically acquired at a rate of 2 ratios per second (i.e., 4 images per second). The ratiometric intensity values were extracted using a custom post-processing program written in Matlab. The program spatially averaged pixel intensities within a region of interest comprising, at least, one half of the length of the artery segment within the field of view that remained the same for both 340 nm and 380 nm images (see ESI Table S7.3 for programmed experimental sequence).

3. Results

In this section, we introduce results obtained from two case studies that were obtained using the artery-on-a-chip platform: one corresponding to end-point measurements and one for time resolved assessment of blood vessel structure and function. The case studies serve to illustrate the utility and consistent operation of the presented platform for the automated, multimodal assessment of blood vessel structure and function.

First, we successfully demonstrated the fixation, permeabilization and staining of SMCs with the goal of directly visualizing proteins and assessing SMC alignment, size and shape. Information regarding the cellular organization is an important indicator of pathological changes resulting from, e.g., vascular remodelling.⁴³ Table S7.1 in the ESI summarizes the 8 step, 4.37 hr experimental sequence that was absolved by computer control, without the

need for manual intervention. Once the artery was loaded on the device each reagent was automatically superfused based on the preprogrammed protocol. The acquired images were rotated such that the artery centerline was oriented vertically using straight channel features of the microfluidic device within the field of view. Ellipses were manually fitted to represent individual SMC nuclei. Using a custom matlab program, the major and minor axes of each ellipse were determined, along with the pitch of the major axis (for more detail see ESI Section S7, particularly Fig. S7.2). Figure 4A shows a representative image of a nuclear stain from which SMC alignment and eccentricity were obtained. SMC eccentricity was quantified by fitting an ellipse to the intensity distribution associated with each stained nucleus. The alignment of the major axis of the ellipse was represented by an arrow, as shown in Fig. 4B. We obtained a pitch of $-0.3^\circ \pm 3.4^\circ$ (Fig. 4C) and an eccentricity with respect to the circumferential direction of 0.991 ± 0.006 (Fig. 4D) from 98 nuclei that originating from $n = 6$ different mouse olfactory artery. The obtained values are consistent with previous reports.⁴⁴

⁴⁵ Figure 4E shows the combined results from F-actin and DAPI staining. In addition to a structural protein, we performed automated immunofluorescence staining of the voltage gated calcium channel Ca_v 1.2, the target of Di-hydropyridine type calcium blockers like nifedipine. The results from absolving an uninterrupted 9 step, 13.95 hr protocol shown in Fig. 4F (for detailed sequence see ESI Table S7.2, for negative control see ESI Fig. S7.3A) indicate a significant expression of the Ca_v 1.2 channel throughout the SMCs of the small artery.

Second, the platform was employed to demonstrate the functional assessment of an olfactory artery segment. Table S7.3 summarizes the experimental sequence that involved 32 automated steps during 3.85 hr. Drugs, buffer and staining reagents were presented to the

chip hosted cerebral artery segment in an automated manner that only required 2 manual steps for purging and refilling select wells on the manifold. The degree of constriction was measured in response to an abluminally applied chemical stimulus of the vasoconstrictor phenylephrine (PE). Vascular constriction due to the application of PE was caused by changes in the calcium concentration within the SMCs. Specifically, PE binds to adrenergic receptors on the SMCs, ultimately resulting in the release of calcium from internal stores and the opening of voltage gated calcium channels. The subsequent intracellular calcium increase is a mandatory signalling event for the constriction of individual SMCs. The cumulative dose dependant constriction of all SMCs produces the functional response of the entire artery. To directly observe changes in intracellular calcium in concert with the constrictor response, the small artery was stained with FURA-2AM. Figure 5A shows a ratiometric calcium image of a chip-hosted and pressurized mouse olfactory artery segment with no PE applied. Pairs of fluorescence images were acquired by illuminating at 340nm and at 380nm, every 0.5s and an intensity ratio was calculated for each image pair. Figure 5B shows the time dependent changes of the F340nm/F380nm ratio (right axis, dashed gray line) and the artery vasomotor response (left axis, solid black line) during phenylephrine stimulation for $n = 5$ artery segments.

The artery was subsequently incubated with the L-type calcium channel blocker Nifedipine and the effects on the measured FURA ratio was measured. Figure 5C compares the initial calcium signal during stimulation with PE (blue colour) with the reduced increase in calcium currents. An approximately twofold reduction of the ratiometric measurement was found for the arteries incubated with the calcium blocker (red colour),^{46, 47} and resulted in a reduced constriction for a given PE concentration. The reduced cellular calcium signalling was

associated with a statistically significant 50% reduction in arterial constriction when treated with Nifedipine (Fig. 5D).^{48, 49}

4. Summary and Discussion

We presented a compact artery-on-a-chip microfluidic platform for the investigation of the structure and function of small intact blood vessels. A multilayer artery-on-a-chip microfluidic device allowed cerebral arteries to be reversibly mounted and subjected to physiological levels of transmural pressure and temperature. The microfluidic device was reversibly interfaced with a custom machined manifold that accommodated six fluid wells along with pneumatic valves for individually controlling the abluminal milieu, along with temperature control. The experimental platform is compact, does not require external syringe pumps, is conveniently interfaced with a standard inverted microscope, and allows functional assessment and staining protocols to be automatically executed after completing a manual loading step.

Three typical applications were demonstrated to highlight the utility of the automated platform. In all three cases, the employed reagent concentrations were comparable to the ones used in standard approaches. However, the total reagent consumption required was reduced by at least one order of magnitude. A maximum of 1ml of combined reagents and buffer, and less than 200 μ l of each reagent, was used during a 10 hour period after the artery was loaded, compared to a typical organ bath volume of 3 ml used in conventional pressure myography setups with reagent that often needs to be replenished during the course of one experiment. First, nuclear and F-actin stains were carried out in a computer controlled manner. Second, automated immunofluorescence stains was used to image the L-type

calcium channel targeted by nifedipine and demonstrated the successful ability to routinely stain and image proteins within the arterial wall.

Third, SMC function and intracellular calcium of mouse cerebral olfactory arteries were simultaneously assessed from dynamically recording bright-field images of the outer diameter (unconstricted diameter $D_o \sim 120 \mu\text{m}$) and ratiometric fluorescence images. After completing a dose-response measurement, vessel constrictor responses were reduced by 50% after the incubation with the calcium blocker nifedipine. The presented concurrent measurements of cellular calcium and arterial tone provide a more comprehensive understanding of vasomotor dynamics by providing access to local calcium elevations and SMC constriction. The substantially reduced manual involvement imposed by our approach, as well as the reproducibility associated with automated functional assessment, tissue processing and abluminal staining of chip-hosted, intact blood vessels may in the future promote systematic studies between subcellular, cellular-level structural characteristics (e.g., protein expression, cell alignment)^{50, 51} to organ-level structure and function. We expect such experimental capacity to be very well suited, e.g., for studies of vascular remodelling. The approach may also be broadly applicable for the combined culture, staining and image-based functional assessment of organs-on-a-chip as well as tissue-engineered vascular constructs.

Acknowledgement

We acknowledge the donation of CYTOP samples by the Asahi Chemical Company, Japan, and Bellex International, Inc (Drs. Kunio Watanabe and Osamu Mihama). Funding from the Natural Sciences and Engineering Council of Canada (Discovery, Discovery Accelerator Supplement (AG) and Phase 2b Idea to Innovation grant (AG, SSB)), from Quorum Technologies (Guelph, ON, Canada) (AG, SSB, John Arbuckle), from the Lilly Research

Award Program (LRAP) (AG, SSB, Dr. Mark D. Rekhter), a fellowship from the NSERC CREATE Program in Microfluidic Applications and Training in Cardiovascular Health (SY), a Barbara and Frank Milligan Graduate Fellowship (SY), and the Wallace G. Chalmers Chair of Engineering Design (AG). Device fabrication was carried out at the Centre for Microfluidic Systems in Chemistry and Biology, funded by Canada Foundation for Innovation and Ontario Research Fund.

References

1. E. M. Lucchetta, J. H. Lee, L. A. Fu, N. H. Patel and R. F. Ismagilov, *Nature*, 2005, **434**, 1134-1138.
2. S. Takayama, E. Ostuni, P. LeDuc, K. Naruse, D. E. Ingber and G. M. Whitesides, *Nature*, 2001, **411**, 1016-1016.
3. C. Moraes, G. Mehta, S. C. Leshner-Perez and S. Takayama, *Annals of Biomedical Engineering*, 2012, **40**, 1211-1227.
4. D. Huh, Y.-s. Torisawa, G. A. Hamilton, H. J. Kim and D. E. Ingber, *Lab on a Chip*, 2012, **12**, 2156-2164.
5. S. N. Bhatia and D. E. Ingber, *Nature Biotechnology*, 2014, **32**, 760-772.
6. P. J. Lee, P. J. Hung and L. P. Lee, *Biotechnology and Bioengineering*, 2007, **97**, 1340-1346.
7. K. Domansky, W. Inman, J. Serdy, A. Dash, M. H. M. Lim and L. G. Griffith, *Lab on a chip*, 2010, **10**, 51-58.
8. B. J. Kane, M. J. Zinner, M. L. Yarmush and M. Toner, *Anal Chem*, 2006, **78**, 4291-4298.
9. S. R. Khetani and S. N. Bhatia, *Nat Biotech*, 2008, **26**, 120-126.
10. D. Huh, B. D. Matthews, A. Mammoto, M. Montoya-Zavala, H. Y. Hsin and D. E. Ingber, *Science*, 2010, **328**, 1662-1668.
11. D. Huh, H. Fujioka, Y.-C. Tung, N. Futai, R. Paine III, J. B. Grothberg and S. Takayama, *Proceedings of the National Academy of Sciences*, 2007, **104**, 18886-18891.
12. N. J. Douville, P. Zamankhan, Y.-C. Tung, R. Li, B. L. Vaughan, C.-F. Tai, J. White, P. J. Christensen, J. B. Grothberg and S. Takayama, *Lab on a Chip*, 2011, **11**, 609-619.
13. K.-J. Jang and K.-Y. Suh, *Lab on a chip*, 2010, **10**, 36-42.
14. K.-J. Jang, H. S. Cho, W. G. Bae, T.-H. Kwon and K.-Y. Suh, *Integrative Biology*, 2011, **3**, 134-141.
15. E. Leclerc, R. g. Baudoin, A. Corlu, L. Griscom, J. Luc Duval and C. c. Legallais, *Biomaterials*, 2007, **28**, 1820-1829.
16. H. J. Kim, D. Huh, G. Hamilton and D. E. Ingber, *Lab Chip*, 2012, **12**, 2165-2174.
17. E. W. Young, M. W. Watson, S. Srigunapalan, A. R. Wheeler and C. A. Simmons, *Analytical Chemistry*, 2010, **82**, 808-816.

18. A. Grosberg, P. W. Alford, M. L. McCain and K. K. Parker, *Lab on a Chip*, 2011, **11**, 4165-4173.
19. J. C. Nawroth, H. Lee, A. W. Feinberg, C. M. Ripplinger, M. L. McCain, A. Grosberg, J. O. Dabiri and K. K. Parker, *Nature Biotechnology*, 2012, **30**, 792-797.
20. H. Shimizu, K. Ohashi, R. Utoh, K. Ise, M. Gotoh, M. Yamato and T. Okano, *Biomaterials*, 2009, **30**, 5943-5949.
21. J. V. Rocheleau, G. M. Walker, W. S. Head, O. P. McGuinness and D. W. Piston, *Proceedings of the National Academy of Sciences of the United States of America*, 2004, **101**, 12899-12903.
22. M. Koenigsberger, R. Sauser, D. Seppely, J.-L. Béný and J.-J. Meister, *Biophysical Journal*, 2008, **95**, 2728-2738.
23. G. S. Jeong, S. Han, Y. Shin, G. H. Kwon, R. D. Kamm, S.-H. Lee and S. Chung, *Analytical Chemistry*, 2011, **83**, 8454-8459.
24. Y. Shin, J. S. Jeon, S. Han, G.-S. Jung, S. Shin, S.-H. Lee, R. Sudo, R. D. Kamm and S. Chung, *Lab on a Chip*, 2011, **11**, 2175-2181.
25. I. K. Zervantonakis, S. K. Hughes-Alford, J. L. Charest, J. S. Condeelis, F. B. Gertler and R. D. Kamm, *Proceedings of the National Academy of Sciences of the United States of America*, 2012, **109**, 13515-13520.
26. M. Montgomery, B. Zhang and M. Radisic, *Journal of Cardiovascular Pharmacology and Therapeutics*, 2014, **19**, 382-393.
27. Y. Xiao, B. Zhang, H. Liu, J. W. Miklas, M. Gagliardi, A. Pahnke, N. Thavandiran, Y. Sun, C. Simmons, G. Keller and M. Radisic, *Lab on a Chip*, 2014, **14**, 869-882.
28. E. W. K. Young and C. A. Simmons, *Lab on a Chip*, 2010, **10**, 143-160.
29. E. S. Hald, K. E. Steucke, J. A. Reeves, Z. Win and P. W. Alford, *Biofabrication*, 2014, **6**.
30. M. Mulvany and W. Halpern, *Nature*, 1976, **260**, 617-619.
31. S. Nogawa, C. Forster, F. G. Zhang, M. Nagayama, M. E. Ross and C. Iadecola, *Proceedings of the National Academy of Sciences of the United States of America*, 1998, **95**, 10966-10971.
32. A. Gunther, S. Yasotharan, A. Vagaon, C. Lochovsky, S. Pinto, J. Yang, C. Lau, J. Voigtlaender-Bolz and S.-S. Bolz, *Lab on a chip*, 2010, **10**, 2341-2349.
33. R. Gomez-Sjoberg, A. A. Leyrat, D. M. Pirone, C. S. Chen and S. R. Quake, *Analytical Chemistry*, 2007, **79**, 8557-8563.
34. S. Takayama, E. Ostuni, P. LeDuc, K. Naruse, D. E. Ingber and G. M. Whitesides, *Chemistry & Biology*, 2003, **10**, 123-130.
35. R. D. Lovchik, G. V. Kaigala, M. Georgiadis and E. Delamarche, *Lab on a Chip*, 2012, **12**, 1040-1043.
36. N. Halidi, F.-X. Boittin, J.-L. Beny and J.-J. Meister, *Cell Calcium*, 2012, **50**, 459-467.
37. D. M. Wang and J. M. Tarbell, *J. Biomech. Eng.-Trans. ASME*, 1995, **117**, 358-363.
38. M. Civelek, K. Ainslie, J. S. Garanich and J. M. Tarbell, *Journal of Applied Physiology*, 2002, **93**, 1907-1917.
39. C. T. Wagner, W. Durante, N. Christodoulides, J. D. Hellums and A. I. Schafer, *Journal of Clinical Investigation*, 1997, **100**, 589-596.
40. S. K. Sia and G. M. Whitesides, *Electrophoresis*, 2003, **24**, 3563-3576.
41. S. Bhattacharya, A. Datta, J. M. Berg and S. Gangopadhyay, *Journal of Microelectromechanical Systems*, 2005, **14**, 590-597.

42. C. Lochovsky, S. Yasotharan and A. Gunther, *Lab on a Chip*, 2012, **12**, 595-601.
43. J. van den Akker, M. J. C. Schoorl, E. Bakker and E. vanBavel, *Journal of Vascular Research*, 2010, **47**, 183-202.
44. M. J. Mulvany and C. Aalkjaer, *Physiological Reviews*, 1990, **70**, 921-961.
45. J. G. Walmsley, R. W. Gore, R. G. Dacey, D. N. Damon and B. R. Duling, *Microvascular Research*, 1982, **24**, 249-271.
46. A. Fleckenstein, *Annual Review of Pharmacology and Toxicology*, 1977, **17**, 149-166.
47. I. Y. Kuo, A. Ellis, V. Al Seymour, S. L. Sandow and C. E. Hill, *Journal of Cerebral Blood Flow and Metabolism*, 2010, **30**, 1226-1239.
48. P. Timmermans, M. J. Mathy, B. Wilffert, H. O. Kalkman, M. Thoolen, A. Dejonge, J. C. A. Vanmeel and P. A. Vanzwieten, *Naunyn-Schmiedebergs Archives of Pharmacology*, 1983, **324**, 239-245.
49. P. Timmermans, A. Dejonge, J. C. A. Vanmeel, M. J. Mathy and P. A. Vanzwieten, *Journal of Cardiovascular Pharmacology*, 1983, **5**, 1-11.
50. N. A. Flavahan, S. R. Bailey, W. A. Flavahan, S. Mitra and S. Flavahan, *American Journal of Physiology-Heart and Circulatory Physiology*, 2005, **288**, H660-H669.
51. G. Gryniewicz, M. Poenie and R. Y. Tsien, *Journal of Biological Chemistry*, 1985, **260**, 3440-3450.
52. A. Dorr, J. G. Sled and N. Kabani, *NeuroImage*, 2007, **35**, 1409-1423.

Figures

Figure 1. Probing smooth muscle structure and function in intact small blood vessels.

(A) Schematic illustration of altering small artery abluminal microenvironment either in real time (diameter change or ion movement) or via end-point analysis (protein expression, phosphorylation). (B) Location of olfactory artery from micro-computed tomographic reconstruction (top left) and magnetic resonance image (top right) of mouse brain vasculature as well as from a combination of both imaging modalities (bottom)⁵². Olfactory artery highlighted in red colour. (C) Schematic representation of cerebral artery structure composed of endothelial cell (EC) layer and several smooth muscle cell (CMS) layers. (D) Schematic illustration of conventional protocol for fixation and abluminal staining. Intact blood vessel segment fixated at time t_0 , embedded in paraffin, sectioned, applied to cover slide, stained, and imaged. (E) Schematic illustration of automated microfluidic approach allowing for fixation and abluminal staining of chip-mounted, pressurized blood vessel segment.

Figure 2. Experimental setup. (A) Schematic illustration of experimental setup for fluidic and temperature control. All liquid lines primed with buffer. Manifold wells (1) initially filled with drug, fixation or staining solutions. Cerebral artery segment manually loaded to inspection area (2) after being inserted into loading well (3). After sealing loading well with lid, fixation pressure P_{fix} hydrostatically applied at both artery ends. Superfusion outlet pressure, P_0 , equal to atmospheric pressure. Superfusion and perfusion inlet pressures, P_{superf} and P_{perf} , set by pressure regulators. Artery temperature controlled via (4) sapphire disk mounted thermoelectric (TE) element and thermistor, and (5) on-chip thin-film resistors. (6) Six manifold mounted pneumatic valves actuate separate on chip valves (7), initiating outflow from wells into superfusion channel. (B) Close-up view of artery inspection area (2). Scale bar 200 μ m. (C) Bright-field image of chip-hosted, pressurized mouse olfactory artery. Scale bar 40 μ m. (D) Schematic cross-section of blood vessel confined between PDMS post arrays on top and bottom walls. (E) Numerically predicted abluminal wall shear stress caused by superfusion cross-flow. (F) Bright-field micrograph of on-chip valve. Red coloured dye indicates (bottom) liquid layer, and green coloured dye (top) pneumatic actuation layer. (G) Thin film resistors for on-chip temperature measurement.

Figure 3 (A) Photograph of manifold with embedded wells, solenoid valves, threaded connections to pneumatic actuation pressures (P_{open} , P_{vac}), perfusion lines, and liquid-filled fixation line. (B) Schematic cross-sectional view of seal established between interconnect (manifold) (top) and elastomeric microfluidic device (bottom) containing fluid with internal pressure P_i . (C) Numerically predicted local deformations of region within dashed box in (B) as compared with un-deformed reference state. Contour lines indicate deformation in micrometers and heatmap color magnitude of normal stress. PDMS substrate with thickness = 4 mm, $\sigma_{seal} = 0.5$ MPa, $P_i = 0$ Pa. (D) Variation of normal stress in x -direction across sealing surface of rim. (E) Schematic of experimental setup for characterization of interconnect. Working fluids are introduced to the custom manifold via threaded ports manifold and standard fluidic connectors. (F) Results from experimental validation of seal

operating envelope as gage pressure of fluid versus the average normal stress applied at the rim of the seal. Error bars correspond to one time the standard deviation.

Figure 4. Fixation and staining of chip-hosted blood vessel. (A) Fluorescence image of pressurized mouse cerebral artery segment after flowable presentation of fixation and staining protocol abluminally (blood vessel center vertical). Elongated SMC nuclei aligned perpendicular to blood vessel. Larger EC nuclei aligned with flow direction. (B) Enlarged view of region A. Best fit ellipse representing SMC nuclei to evaluate eccentricity based on ratio of minor and major axes. Red vectors indicate SMC alignment with respect to horizontal axis (counted positive above horizontal axis). Scale bar 5 μ m. (C) Nuclear orientation characterized by histogram and whisker plot of individual data points. Box extends from 25th to 75th percentile (interquartile range, IQR). Center position indicates median value. Whiskers (error bars) span distance between 10th and 90th percentiles. Points in black colour indicate outliers, i.e., exceeding 1.5 \times IQR. (D) Histogram and whisker plot of nuclear eccentricity. (E) Co-stained F-actin and nuclei chip hosted mouse olfactory artery segment. (F) Immunofluorescence image of Cav1.2 voltage gated calcium channels. All scale bars 40 μ m unless otherwise stated.

Figure 5. On-chip assessment of blood vessel calcium dynamics and vasomotion. (A) False coloured ratiometric calcium image (Hue determined by 380nm image, intensity determined by 340nm image) of Fura-2 stained mouse cerebral artery in the absence of PE. Scale bar 40 μ m. (B) Time evolution of artery outer diameter and calcium response to stepwise increasing phenylephrine (PE) concentration. (C) Change in calcium responses before (blue) and after (red) incubation with calcium blocker nifedipine. (D) Dose dependent vasoconstriction in response to phenylephrine with and without incubation with nifedipine. Error bars represent mean experimental error. Symbol * indicates $p < 0.05$. Error bars correspond do one time the mean experimental error.

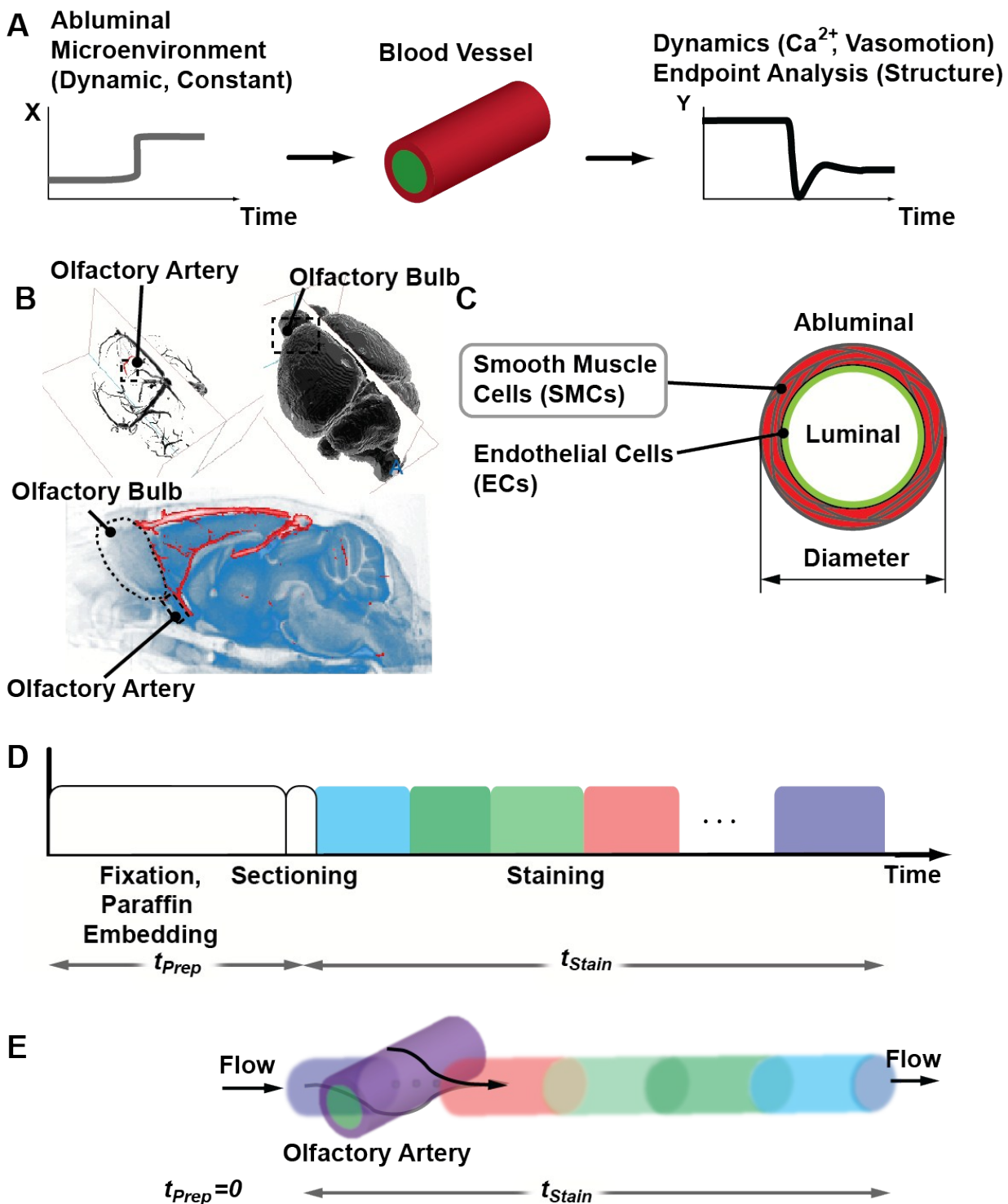


Figure 1

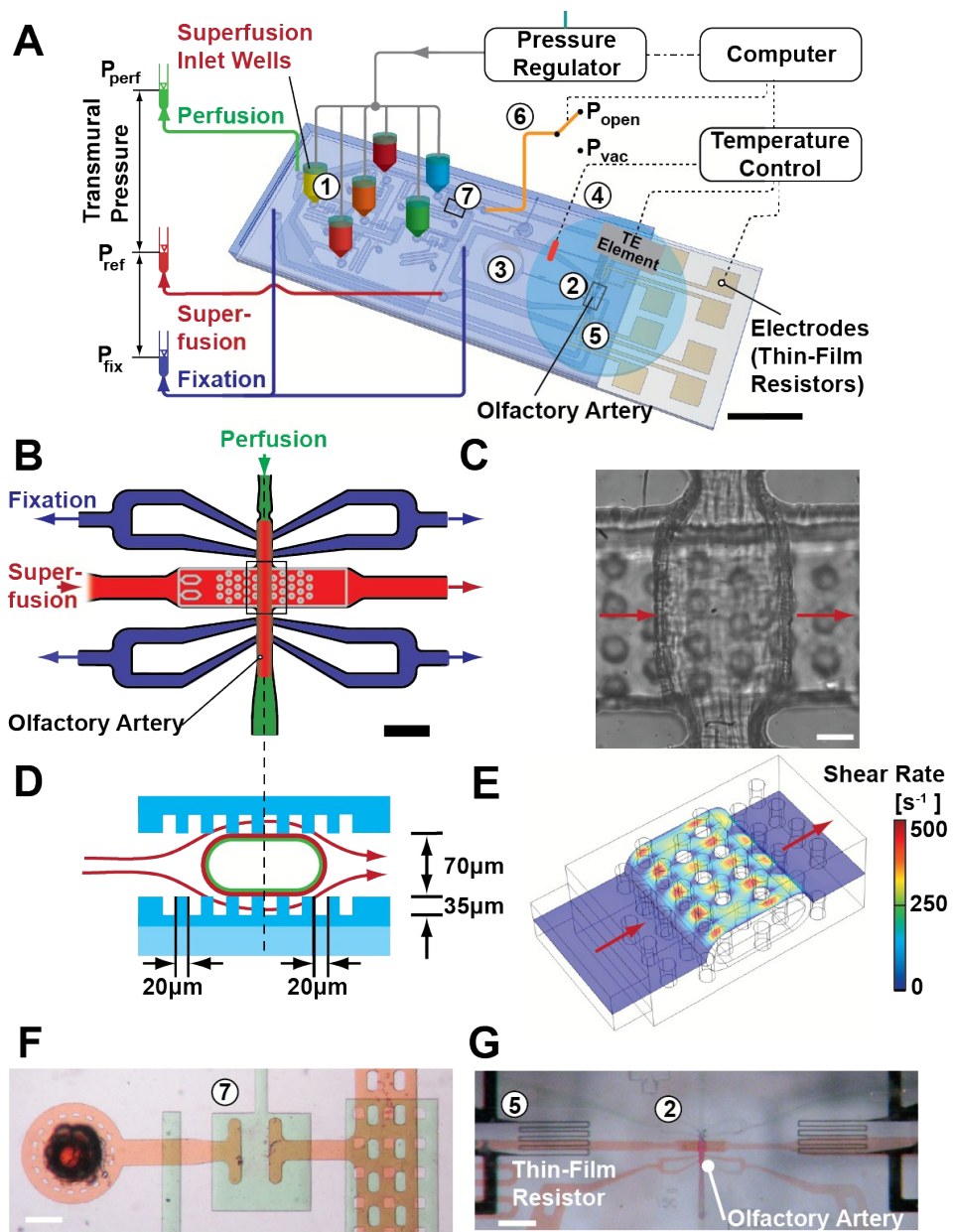


Figure 2

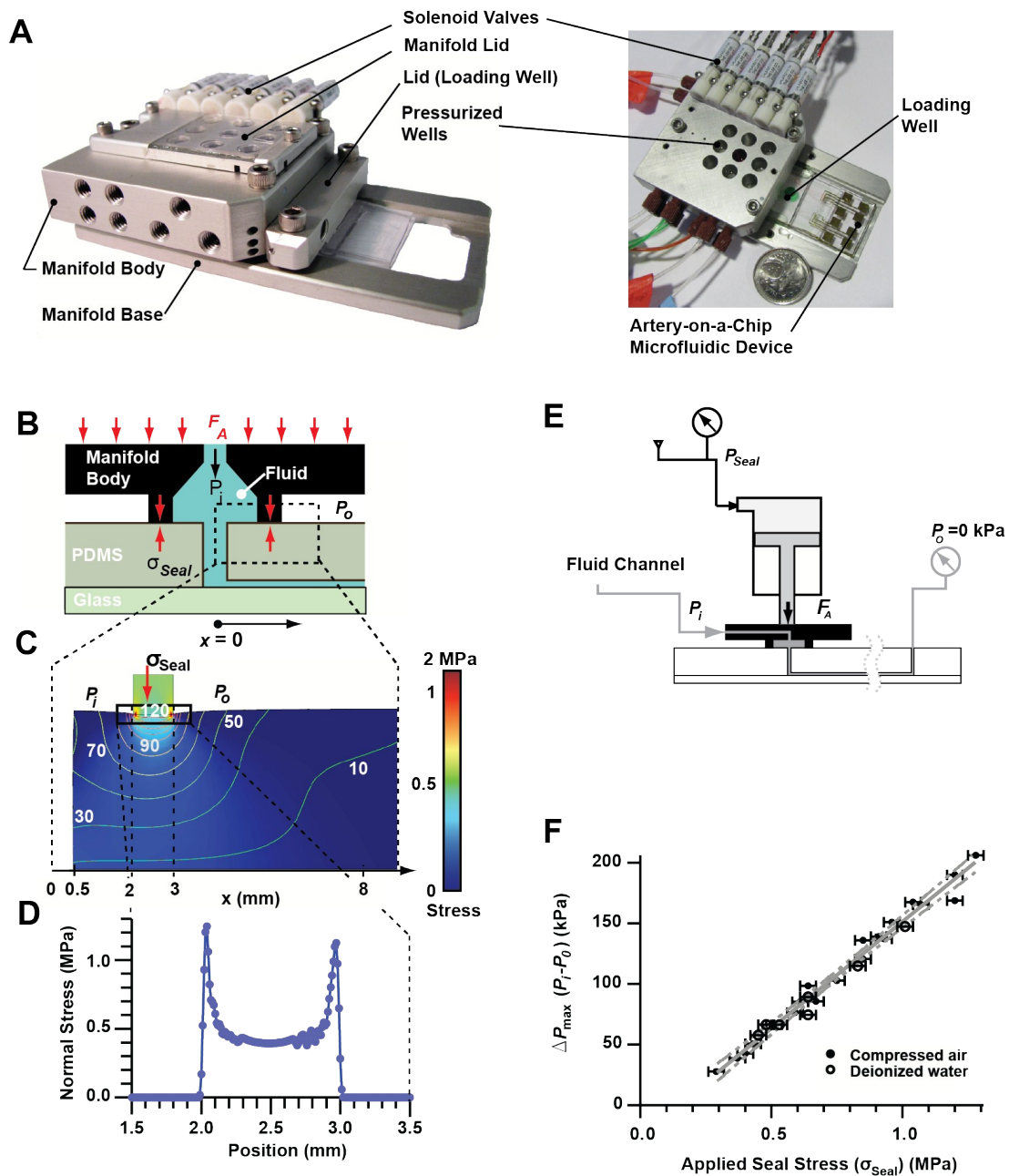


Figure 3

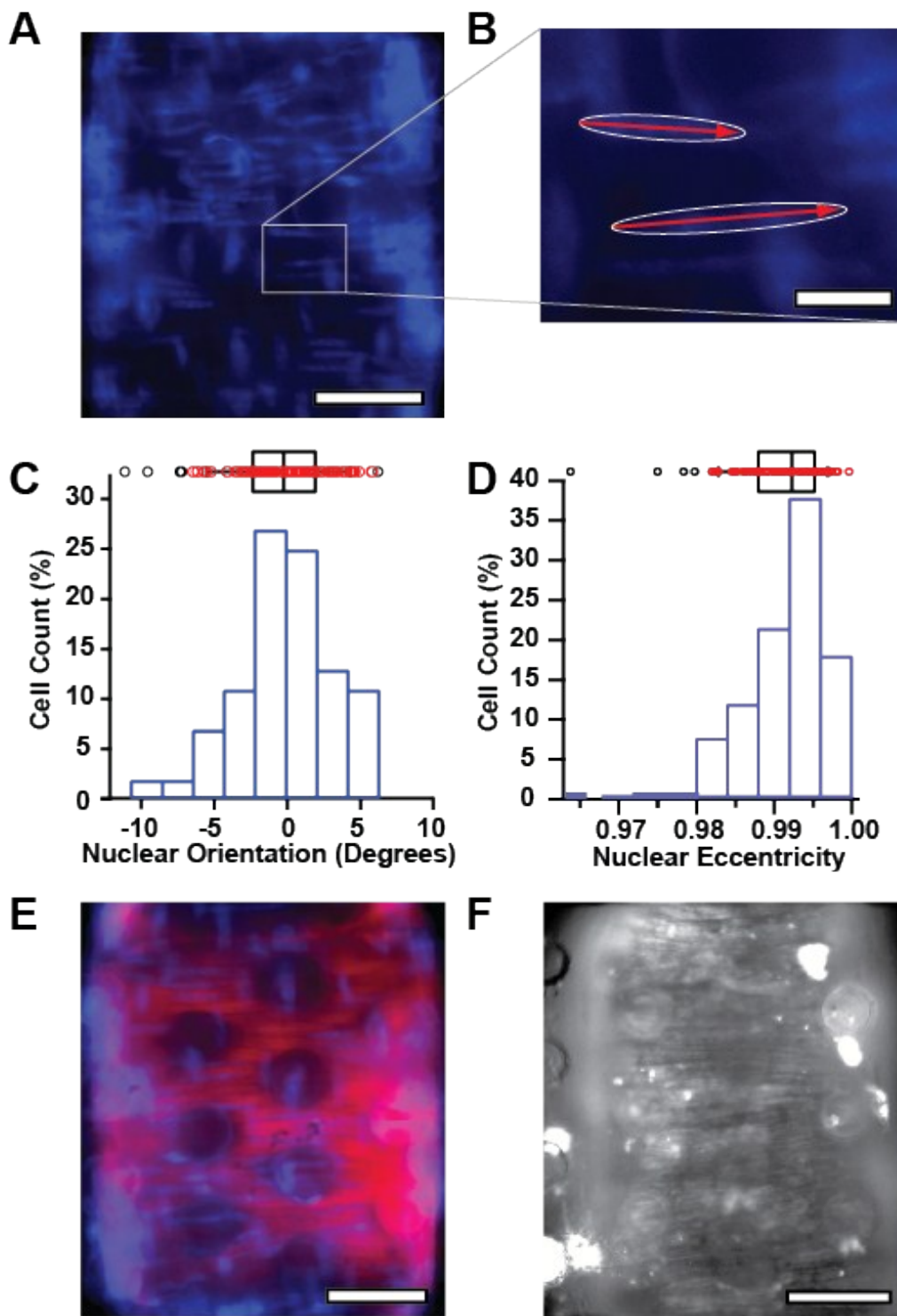


Figure 4

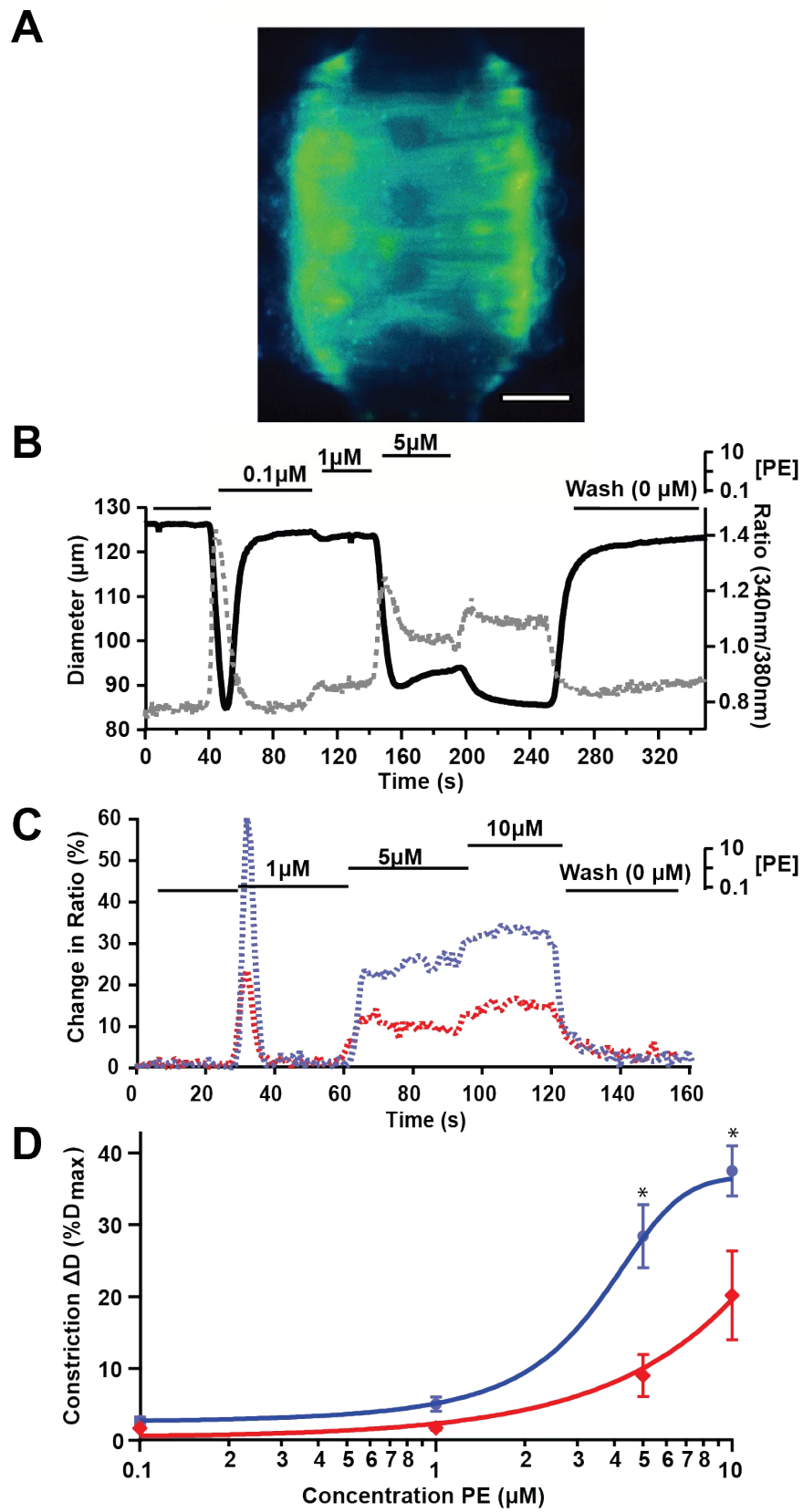


Figure 5